MATERIALS SCIENCE

Mechanochemically accelerated deconstruction of chemically recyclable plastics

Mutian Hua[1], Zhengxing Peng[2], Rishabh D. Guha[1], Xiaoxu Ruan[3], Ka Chon Ng[1], Jeremy Demarteau[4], Shira Haber[1], Sophia N. Fricke[1,5], Jeffrey A. Reimer[1,5], Miquel B. Salmeron[1,4], Kristin A. Persson[1,3,4], Cheng Wang[2], Brett A. Helms[1,4]*

Plastics redesign for circularity has primarily focused on monomer chemistries enabling faster deconstruction rates concomitant with high monomer yields. Yet, during deconstruction, polymer chains interact with their reaction medium, which remains underexplored in polymer reactivity. Here, we show that, when plastics are deconstructed in reaction media that promote swelling, initial rates are accelerated by over sixfold beyond those in small-molecule analogs. This unexpected acceleration is primarily tied to mechanochemical activation of strained polymer chains; however, changes in the activity of water under polymer confinement and bond activation in solvent-separated ion pairs are also important. Together, deconstruction times can be shortened by seven times by codesigning plastics and their deconstruction processes.

INTRODUCTION

Closed-loop chemical recycling of plastic waste to reusable monomers can be undertaken with low carbon and energy intensity when mechanically recycled plastics are deconstructed as solids, suspended in a liquid reaction medium (*1*–*9*). During deconstruction, various species from the reaction medium partition into amorphous regions within the polymer, swelling the polymer and triggering chemical transformations therein. Yet, it remains a challenge to monitor and track reactions occurring in solvated polymer solids, leaving opaque the effects of polymer-solvent interactions on polymer reactivity.

Here, we show by using in situ near-edge x-ray absorption fine structure (NEXAFS) and nuclear magnetic resonance (NMR) spectroscopic analyses that the rate of polymer deconstruction, thought to be dictated exclusively by monomer designs (*10*–*12*), is substantially higher when the polymer chains are stretched, due to swelling in the reaction medium. Furthermore, by exploiting kosmotropic (stabilized hydrogen bonding between water molecules) and chaotropic (disrupted hydrogen bonding between water molecules) counterions in the reaction medium to control the degree of swelling, we can modulate the extent of mechanochemical activation of cleavable bonds at the network level in circular plastics, increasing initial rates by sixfold. Concurrent with these effects, in situ Raman spectroscopy studies and molecular dynamics (MD) simulations show that counterions further influence deconstruction rates at the molecular level by altering the structure of water near the sites of bond cleavage, which dictates the extent of bond activation toward hydrolysis. By understanding these combined effects across scales, we reveal compelling, nonobvious pathways for expediting polymer deconstruction: Mechanochemical activation of hydrolyzable bonds enables faster conversion of swollen polymer solids to dispersed particulates in reactive liquid media, which should be explicitly tailored to maximize hydrolysis rates yielding reusable monomers in high yields through bond activation in smaller molecular fragments (Fig. 1A).

This understanding is a departure from conventional wisdom that might otherwise seek to explain polymer reactivity using theoretical insights or kinetic studies of small-molecule models, which rarely consider the combined influence of heterogeneity, macromolecular architecture, chain conformation, solvation, and speciation (*10*, *11*, *13*–*17*). Furthermore, observations that mechanochemical activation of bonds in swollen polymers is important during the early stages of polymer deconstruction provide lines of intrigue for mechanochemistry and its potential role in informing plastics redesign for circularity (*18*–*21*). We also find that the selection of a reaction medium itself would benefit from the breadth of knowledge guiding the use of kosmotropic and chaotropic ions when seeking control over solvation (*22*, *23*), nucleation (*24*–*26*), and crystallization (*27*–*29*), particularly in water-participating catalytic deconstruction reactions (*30*, *31*). Doing so ensures that oligomer intermediates in chemical recycling of plastics can be more efficiently deconstructed to monomers at high rates and in high yields. This knowledge, when combined with information regarding the structure and activity of water alongside solvation-induced mechanochemical activation of polymer bonds, provides an unexpectedly clear vantage point that captures the underlying phenomena responsible for polymer deconstruction across scales and opens the door to design concepts exploiting these behaviors in future plastics to enhance and ensure their recyclability.

RESULTS

Modular platform for controlling polymer swelling in acidolytic media

Polydiketoenamines (PDKs) are an emerging family of highly recyclable polymers that are poised to replace several classes of difficult-to-recycle polymers, such as epoxy and polyurethane resins. PDKs are synthesized from a diverse array of polytopic triketone and amine monomers via "click" polycondensation reactions (*8*). Segmental chain flexibility inherent to many polyetheramines enables

[1]Materials Sciences Division, Lawrence Berkeley National Laboratory, Berkeley, CA 94720 USA. [2]Advanced Light Source, Lawrence Berkeley National Laboratory, Berkeley, CA 94720 USA. [3]Department of Materials Sciences and Engineering, University of California, Berkeley, Berkeley, CA 94720 USA. [4]The Molecular Foundry, Lawrence Berkeley National Laboratory, Berkeley, CA 94720 USA. [5]Department of Chemical and Biomolecular Engineering, University of California, Berkeley, Berkeley, CA 94720 USA.
*Corresponding author. Email: bahelms@lbl.gov

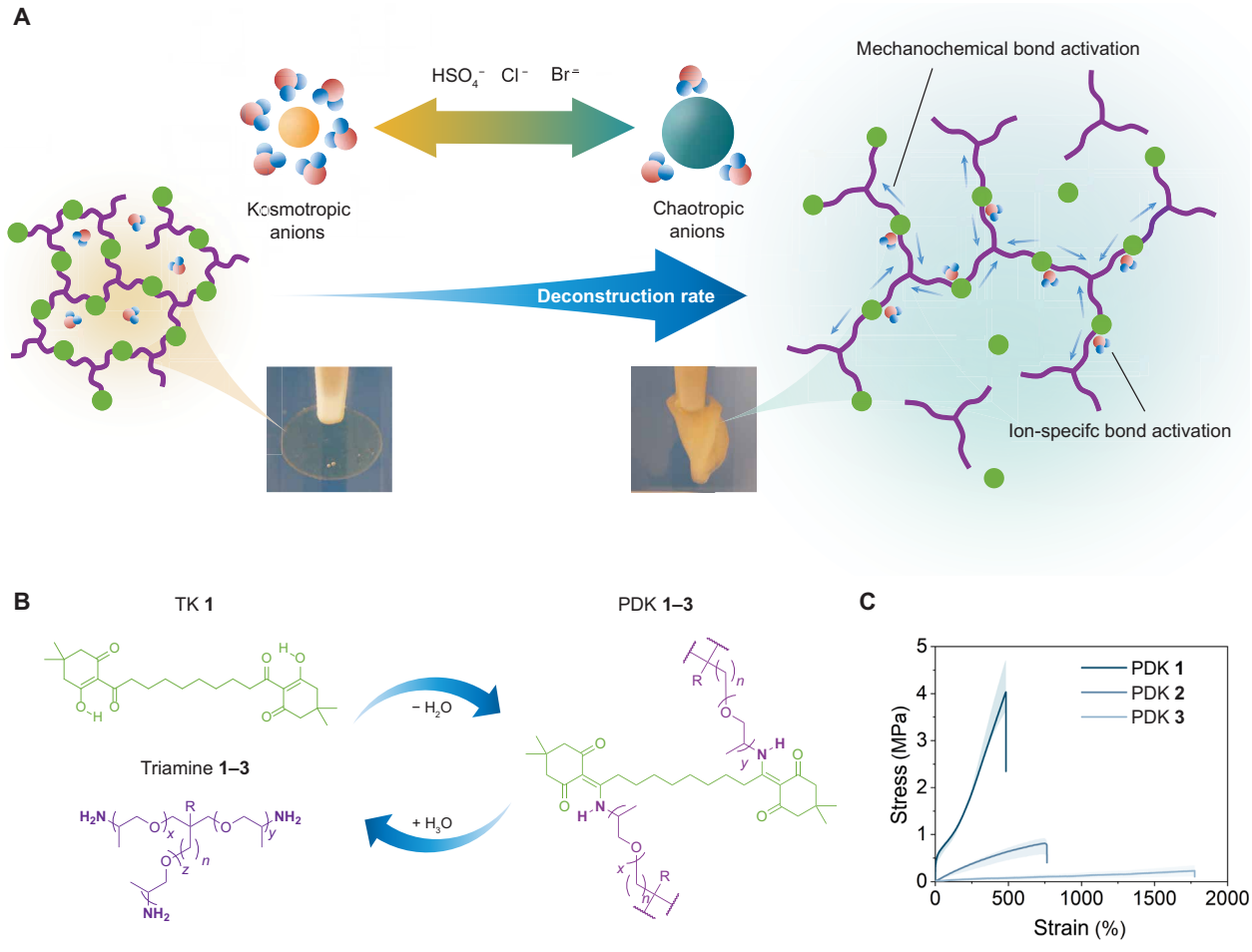

Fig. 1. Enabling circularity in plastics by accelerating polymer deconstruction across scales. (**A**) At early stages of heterogeneous polymer deconstruction, controlling the swelling of polymer chains is key to accelerating reaction rates for bond hydrolysis. At longer timescales, the structure of water near the remaining hydrolyzable bonds in the dispersed solids dictates rates through hydrogen bond-mediated bond activation. The acid counterion plays distinct roles during each phase of deconstruction: The chaotropicity of the anion can be exploited to control swelling, while its ability to engage in hydrogen bonding with water affects the solvation environment near the bond undergoing hydrolysis. The inset photos showed the appearance of PDK elastomer discs clamped by tweezers undergoing deconstruction in 5.0 M H_2SO_4 (left) and 5.0 M HBr (right) for 12 hours under ambient temperature. (**B**) Chemical structure of TK **1** monomer (left, green), triamine **1** to **3** (left, purple) monomer, and the circular PDK elastomers (right). Triamine **1** is slightly different in its chemical structure compared to triamines **2** and **3**. R is hydrogen, and *n* is 1 for triamine **1**. R is an ethyl group, and *n* is 0 for triamines **2** and **3**. (**C**) Tensile stress-strain curves of PDK elastomers **1** to **3**. Error bars were calculated as the SD from the mean for three independently tested samples for each PDK formulation.

the creation of PDK elastomers that swell in acidolytic media, returning reusable monomers with high yield and purity (*32*). Lacking, however, has been a means to control the extent of PDK swelling in an aqueous acid, which may depend on cross-linking density and the choice of acid.

To create PDK elastomers **1** to **3** with controlled cross-linking density, we combined a simple ditopic triketone monomer (TK **1**) (*8*) with either one of three tritopic amine-terminated polypropylene glycol cross-linkers (triamines **1** to **3**) (*33*), whose number-average molar masses were M_n ~ 440, 3000, and 5000 g mol^{-1}, respectively (Fig. 1B and figs. S1 to S3). PDK elastomers **1** to **3** therefrom were flexible with glass transition temperature (T_g) in the range of 17° to −60°C and decomposition temperature (T_d) in the range of 272° to 328°C (figs. S4 and S5). These elastomers exhibited a broad range of mechanical properties, including tensile strength up to 4.02 ± 0.68 MPa and tensile strain up to 1730 ± 350%, similar to commercial epoxy resins and highly stretchable elastomers (Fig. 1C) (*34*, *35*). However, PDK elastomers **1** to **3** are distinctive from commercial materials in that they are thermally reprocessible and chemically recyclable in a fully closed loop (figs. S6 and S7) (*9*).

Mechanochemical acceleration of polymer network deconstruction

To differentiate the reactivity of polymers (Fig. 2A) from small molecules (Fig. 2B) during deconstruction, we carried out in situ NEXAFS in an x-ray transparent liquid cell to monitor initial rates of acidolysis in solid PDK elastomers in contact with a prescribed amount of an aqueous acid. Aqueous acid ionizes diketoenamine functionalities constituting the network, which in turn swells the polymer, in advance of hydrolysis reactions that ultimately generate triketone and triamine products. At ambient temperature, the hydrolysis reaction for this specific PDK network is slow, such that the

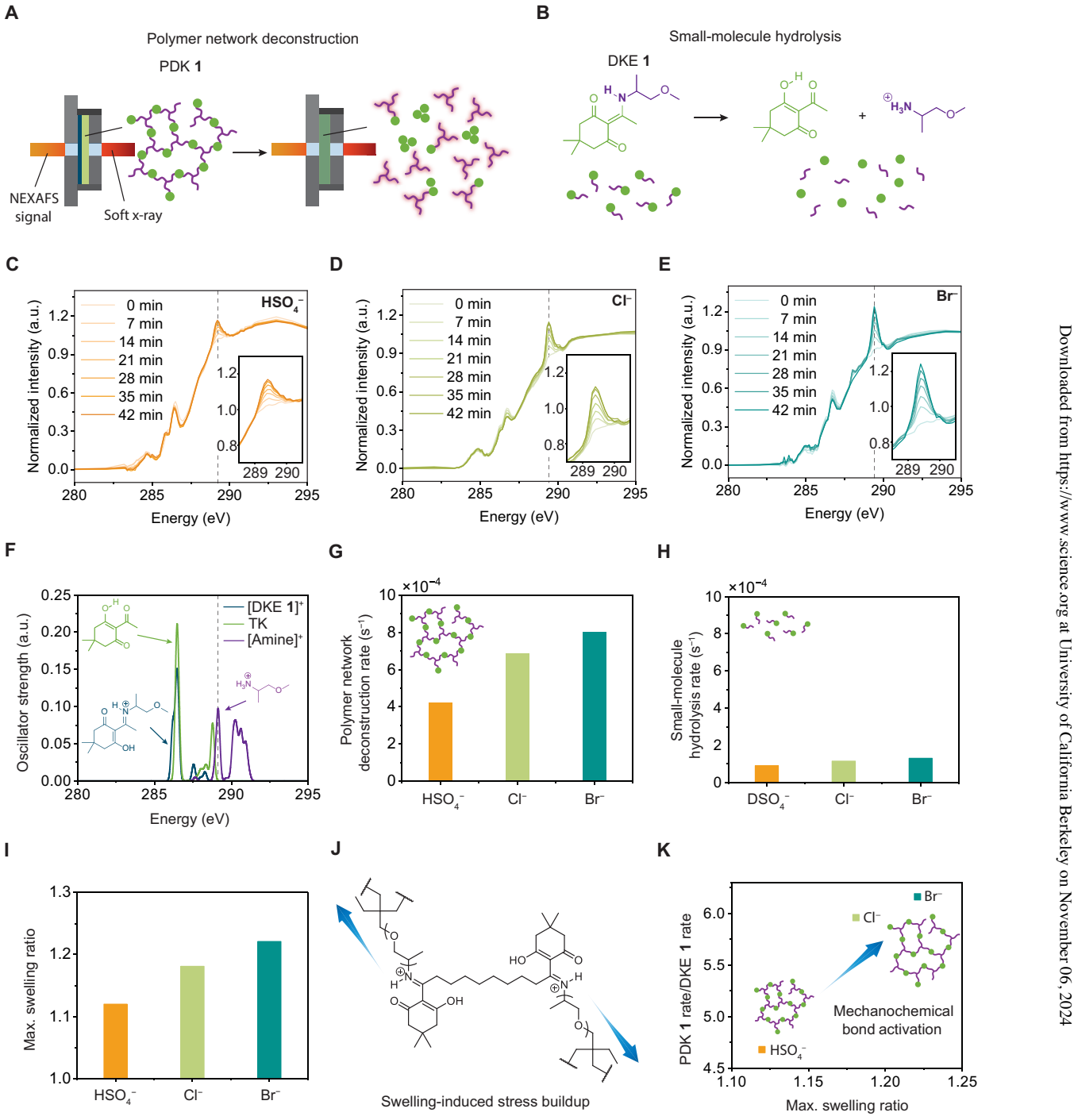

Fig. 2. Mechanochemical activation of hydrolyzable bonds in solvated polymer networks. (**A**) Illustration of the deconstruction of PDK elastomers during in situ NEXAFS measurements. (**B**) Illustration of the deconstruction of DKE **1**, a small-molecule analog of the hydrolyzable bond in PDK elastomers. (**C** to **E**) Overlaid NEXAFS spectra of PDK **1** undergoing deconstruction in 5.0 M H_2SO_4, HCl, and HBr at 60°C. a.u., arbitrary units. (**F**) TD-DFT–simulated NEXAFS spectrum of protonated DKE **1**, 2-acetyl-5,5-dimethyl-1,3-cyclohexanedione (TK), and 1-methoxy-2-propylamine, the acidolysis product of DKE **1**. (**G**) Deconstruction rates of PDK **1** in 5.0 M H_2SO_4, HCl and HBr at 60°C. (**H**) Deconstruction rates of DKE **1** in 5.0 M D_2SO_4, DCl, and DBr at 60°C. (**I**) Maximum swelling ratio of PDK **1** during deconstruction in 5.0 M H_2SO_4, HCl, and HBr at 60°C. (**J**) Mechanochemical acceleration of diketoenamine acidolysis in solvated polymer networks. (**K**) Ratio of deconstruction rates at 60°C for PDK **1** and DKE **1** as a function of PDK elastomer swelling ratio in different acidolytic media.

x-ray setup can be mounted without the PDK film experiencing significant chemical changes until triggered at the elevated temperature. The sensitivity of our methodology is dictated by the prevalence of spectroscopically distinctive chemical functionality in the reactants, intermediates, and products. Accordingly, we chose to study the effects of the reaction medium on deconstruction behaviors of elastomeric PDK **1**, owing to its higher concentration of diketoenamine bonds. To this end, we observed PDK **1** network deconstruction over 45 min at 60°C, varying the acid as follows: 5.0 M H_2SO_4, 5.0 M HCl, and 5.0 M HBr (Fig. 2, C to E). Before these experiments, we carried out extensive studies, modulating the incident x-ray flux to understand how best to minimize radiation damage to the sample and the volume of acid added to the in situ cell to ensure that the signal-to-noise ratio was adequate (fig. S8).

To interpret the data, we assigned features in the NEXAFS spectra by comparing them to simulated spectra for small-molecule analogs of reactants, intermediates, and products by using time-dependent density functional theory (TD-DFT) (Fig. 2F and figs. S9 and S10) (*36*). We assigned the most prominent feature at 289.4 eV to C–N bonds exclusively present in liberated polyetheramine cross-linkers (i.e., acidolysis products), which enabled quantification of acidolysis rates. In contrast, less prominent features at 286.6 eV, corresponding to C=O bonds, were assignable to either diketoenamine moieties in PDK **1** to **3** (reactants) or liberated β-triketones (products) and therefore less than ideal for precise quantification. To determine the initial rates of diketoenamine acidolysis, we thus calculated the peak areas at 289.4 eV and fit the data to a model for pseudo-first-order reaction kinetics (fig. S11). To our surprise, the initial rates for PDK deconstruction varied substantially by the composition of the acidolytic reaction medium: Relative to the initial rate for PDK **1** deconstruction in 5.0 M H_2SO_4 ($-d[\mathrm{DKE}]/dt = 4.22 \times 10^{-4}\ s^{-1}$), those for its deconstruction in 5.0 M HCl and HBr were 62 and 90% faster, respectively (Fig. 2G).

To clarify the origin of rate acceleration, we assessed by variable-temperature ^{1}H NMR the initial rates of diketoenamine acidolysis for an analogous small-molecule diketoenamine, DKE **1**, dissolved in each of the different acids. We conducted these studies at temperatures of 40°, 60°, and 80°C, extracting the initial rates and then fit the data to a pseudo-first-order kinetics model (Fig. 2H and figs. S12 to S14). The initial rates of hydrolysis for DKE **1** at 60°C showed a similar trend as PDK **1** regarding anion type: Relative to the initial rate for DKE **1** hydrolysis in 5.0 M D_2SO_4 ($-d[\mathrm{DKE}]/dt = 0.90 \times 10^{-4}\ s^{-1}$), those for DKE **1** hydrolysis in 5.0 M DCl and DBr were 27% and 44% faster, respectively. Yet, most notably in all cases, the initial rates of PDK **1** deconstruction (Fig. 2G) were substantially higher than the rates for DKE **1** in a given acidolytic medium at a prescribed temperature (Fig. 2H), despite DKE **1** having more degrees of freedom as a dissolved solute than a diketoenamine bond would when part of a polymer network. In the presence of kosmotropic anions (HSO_4^-), the initial rate of PDK **1** deconstruction was 470% that of DKE **1**, and in the presence of chaotropic anions (Cl^-, Br^-), this ratio increased sixfold. The high contrast of rates between PDK **1** and DKE **1** and the relatively low contrast of rate between kosmotropic (HSO_4^-) and chaotropic anions (Cl^- and Br^-) suggested an acceleration mechanism that can be influenced by the type of anions but only present in a polymer network.

While the origin of this rate acceleration was not immediately clear, we observed differences in the degree of swelling depending on the acid type. Solvent uptake in polymer networks leads to the development of stress to balance the decrease in entropy (*18*, *19*), thus a higher degree of swelling generates higher stress in the polymer network. Connecting the trend of swelling and rate of polymer deconstruction could imply a mechanochemical effect introduced by the kosmotropic or chaotropic characters of the different acid anions (*22*, *37*). Consistent with this line of reasoning, the maximum swelling ratio increased in the order of HSO_4^-, Cl^-, and Br^- (Fig. 2I and fig. S15). It is generally accepted that less solvated chaotropic anions (Cl^- and Br^-) are driven to polymer-water interfaces, which, in this case, enhances swelling via more favorable solvation thermodynamics (*23*). Most notably, we found a strong positive correlation between the ratios of initial rates of diketoenamine bond hydrolysis in networked PDK **1** to those of small-molecule DKE **1** in different acidolytic media as a function of the swelling ratio. Thus, solvation of polymer networks leads to pronounced mechanochemical activation of hydrolyzable bonds as the major rate acceleration mechanism during early stages of polymer network deconstruction, regardless of the acid type; this effect is most pronounced in acidolytic media in which chaotropic anions collude with water to swell the network to the greatest extent (Fig. 2, J and K). While not explicitly studied here, it may also be the case that the location of the cross-linking diketoenamine functionality along polyether chains (i.e., at a location other than the chain end) could be a further lever to tune the extent of tension-coupled effects on bond activation.

Likewise noteworthy is the apparent influence of anion type on acidolysis rates for small molecules featuring a diketoenamine bond (i.e., DKE **1**) (Fig. 2H), which will gradually become the dominant factor for rate acceleration as the polymer network breaks down into smaller oligomers. The rate acceleration attained by changing acid anions was even more prominent when less thermal activation was provided. By decreasing the acidolysis temperature to 40°C, the initial rates of DKE **1** hydrolysis in 5.0 M DCl and DBr were 180 and 290% faster, respectively, than in 5.0 M D_2SO_4 (fig. S12), compared to a maximum of 44% attained at a temperature of 60°C (Fig. 2H and fig. S13). This persistent rate acceleration tied directly to anions even in the absence of a strained polymer network necessitates further study into its acceleration mechanisms.

Understanding bond activation in solvent-separated ion pairs

To understand the apparent role of acid type on molecular diketoenamine hydrolysis rates (Fig. 2H and figs. S12 to S14), we considered the effects of solvation and ion pairing as well as the activity of water and their relation to bond activation in the rate-limiting step, where water adds to an iminium intermediate along the reaction coordinate. It was clear from the standard free energies of activation ($\Delta G^{\ddagger}$) for DKE **1** hydrolysis—which were extracted from temperature-dependent ^{1}H NMR kinetics experiments (Fig. 3A and fig. S16)—that the energy landscape for diketoenamine hydrolysis was substantially altered in different acidolytic media. We carried out MD simulations of DKE **1** in those media (i.e., with explicit solvent and acid molecules) and revealed solvent-separated ion pairs, where a single water molecule was simultaneously bound to the iminium and any of the chaotropic halide ions through a series of hydrogen bonds (DKE **1** N–H···O; Fig. 3, B to D). Furthermore, with increasing chaotropicity of the halide ions, we found that the number of hydrogen bonds between water molecules (solvent H–O···H) was reduced (Fig. 3B), which is concomitant with an increase in the

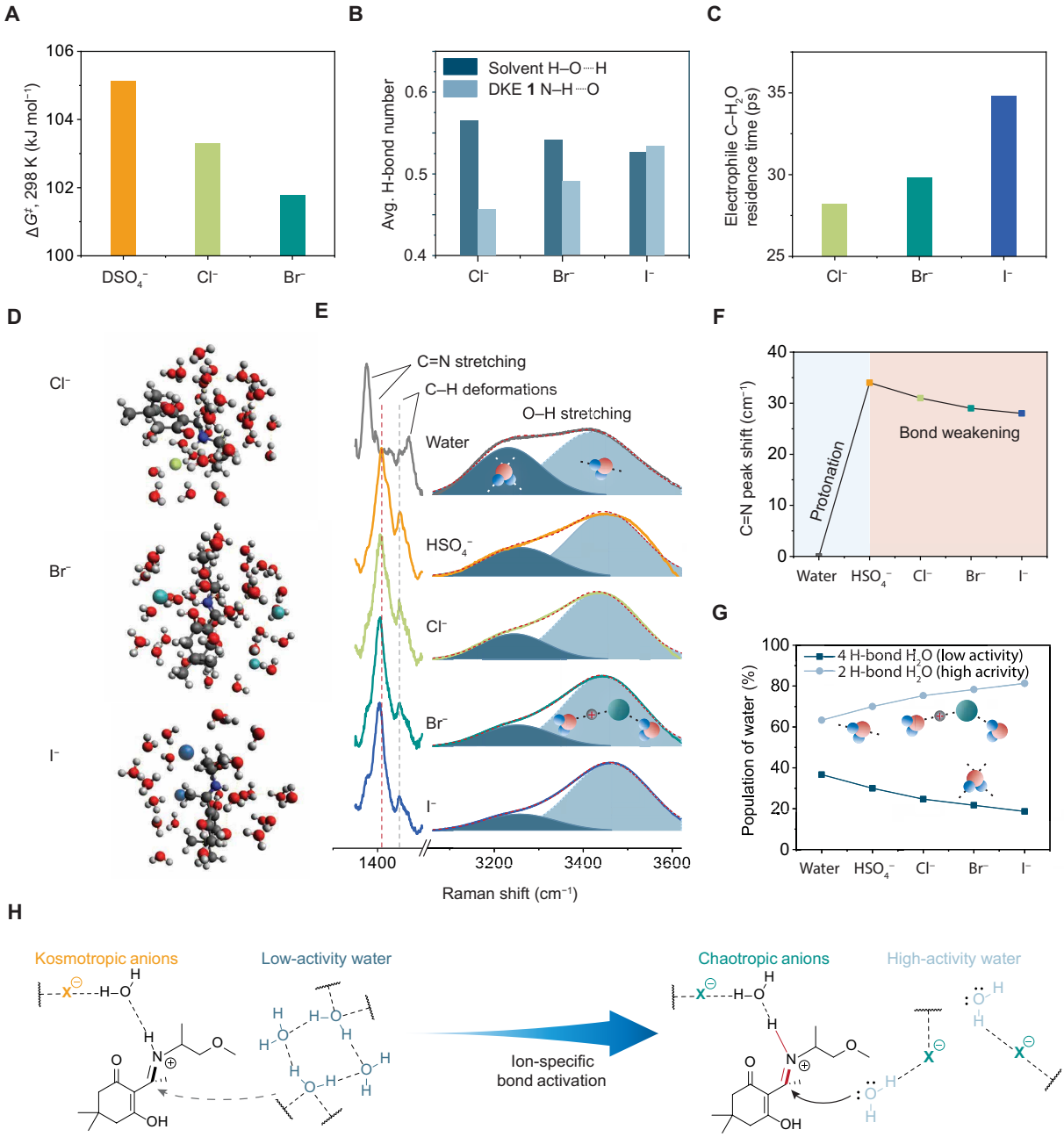

Fig. 3. Matched high water activity and diketoenamine bond activation in solvent-separated ion pairs. (**A**) Experimentally determined $\Delta G^{\ddagger}$ for DKE **1** hydrolysis in 5.0 M D_2SO_4, DCl, and DBr. (**B**) Average number of hydrogen bonds (H-bond) per water molecule in bulk solvent, per DKE **1** near the iminium obtained from MD simulations. (**C**) Water residence time at the electrophile carbon of DKE **1** obtained from MD simulations. (**D**) Snapshots of the MD simulations for DKE **1** in different acidolytic media. (**E**) Raman spectra of DKE **1** in deionized water and 5.0 M H_2SO_4, HCl, HBr, and HI. Gaussian distributions are shown in blue for species of water with different hydrogen bonding configurations. The red dashed line is the fitted spectrum, combining the two Gaussians. (**F**) Shifts of the C=N peak as a function of anion type. (**G**) Population of 4 H-bond water and 2 H-bond water as a function of anion type. (**H**) Illustration of bond activation due to the change in the structure of water. In the presence of chaotropic anions, stronger hydrogen bonds are formed between it, bound water, and the out-of-plane iminium species in solvent-separated ion pairs after the diketoenamine undergoes ionization in acid. Less hydrogen-bonded water also exhibits higher activity during acidolysis.

activity of water toward participating in hydrolysis reactions, owing to the greater availability of oxygen lone pair electrons. Concurrently, the residence time of water molecules at the reaction center was increased (Fig. 3C). The confluence of increased bond activation in solvent-separated ion pairs, higher water activity, and longer residence time near bonds undergoing hydrolysis produced improved kinetics as well as thermodynamics for acidolysis with increasing chaotropicity of the acid anions.

Supporting these simulations, we found by Raman spectroscopy of DKE **1** in 5.0 M acid solutions (Fig. 3E) that the ionization of the diketoenamine bond is evident in the blue shift of the feature at 1375 cm^{-1} (characterized in water) to 1403 to 1410 cm^{-1} (characterized

in acids), which was assigned to the C=N bond. With increasing chaotropicity of the acid anion (HSO_4^- < Cl^- < Br^- < I^-), the C=N bond was weakened, characterized by an increasing red shift in the peak position relative to the same peak observed in the least chaotropic acid (HSO_4^-) and therefore was more susceptible toward hydrolysis (Fig. 3F). This is consistent with stronger hydrogen bonds in solvent-separated ion pairs, i.e., anion–water–NH (iminium) (*38*, *39*) . We also observed changes in the structure and activity of water in the region of 3100 to 3700 cm^{-1}. The O–H stretching band in all samples was composed of two principal components: the first at ~3200 cm^{-1}, corresponding to tetrahedral water with four hydrogen bonds (4 H-bond H_2O); and the second at ~3440 cm^{-1}, corresponding to water with two hydrogen bonds (2 H-bond H_2O) (*40*, *41*). With increasing chaotropicity of the anions, the tetrahedral structure of water was increasingly disrupted (*40*, *42*), as indicated by the diminution in the peak around 3200 cm^{-1}; the prevalence of higher-activity 2 H-bond H_2O features was increasingly dominant (Fig. 3G). This observation was further corroborated by diffusion-ordered spectroscopy (table S1) characterization of the same system, where increasing chaotropicity of the acid anion led to increased diffusivity of hydroniums in the reaction medium, as a result of the increased activity of water (*43*). Thus, stronger H-bonds in solvent-separated ion pairs weaken the hydrolyzable iminium bond, activating it toward acidolysis, while the structure of water is reorganized to show higher activity, promoting acidolysis (Fig. 3H).

Impacts of accelerated deconstruction across scales on monomer recovery

Understanding the implications of bond activation at these two length scales, we sought to control deconstruction of PDK elastomers by exploiting their interactions with the acidolytic reaction medium. At 60°C, PDK **1** underwent deconstruction at different rates in 5.0 M HBr, HCl, and H_2SO_4, which resulted in the progressive formation of smaller PDK solids (process 1) and, ultimately, colorless triketone precipitates (process 2) (Fig. 4A). While processes 1 and 2 take place concurrently during PDK deconstruction, here we delineated the two processes for clarity of discussion. Processes 1 and 2 of PDK **1** deconstruction were fastest in 5.0 M HBr, where after only 1 hour, the triketone monomer had begun to precipitate from the reaction mixture; in 5.0 M HCl, this onset took 2 hours; in 5.0 M H_2SO_4, 3 hours was required. While we observed similar trends with acid composition for PDK **2** (fig. S17) and PDK **3** (Fig. 4B), it was notable that process 1 was slower overall for networks with lower cross-linking density. Therefore, polymer networks with low cross-linking density (and concomitantly low volume fractions

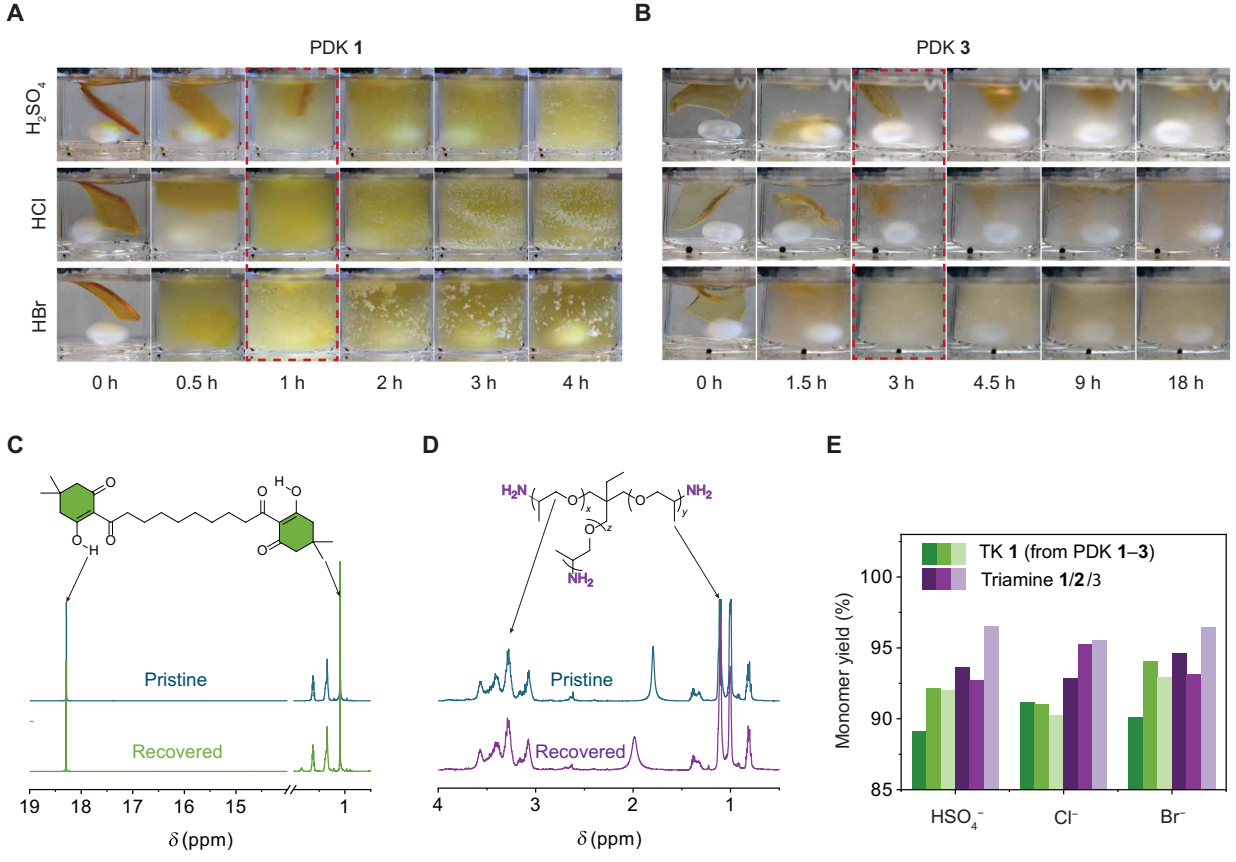

Fig. 4. Ion-specific effects in PDK deconstruction in acid. (**A**) Snapshots of PDK **1** undergoing acidolytic deconstruction in 5.0 M H_2SO_4, HCl, and HBr at 60°C. (**B**) Snapshots of PDK **3** undergoing acidolytic deconstruction in 5.0 M H_2SO_4, HCl, and HBr at 60°C. (**C**) ^{1}H NMR spectrum of pristine (top) and recovered (bottom) TK **1** from PDK **1** deconstructed in 5.0 M HCl at 60°C. ppm, parts per million. (**D**) ^{1}H NMR spectrum of pristine (top) and recovered (bottom) triamine **1** from PDK **1** deconstructed in 5.0 M HCl at 60°C. (**E**) Yields of recovered TK **1** and triamines **1** to **3** from PDK **1** to **3**, respectively, deconstructed in 5.0 M H_2SO_4, HCl, and HBr at 60°C.

of ionizable functionality contributing to swelling) require tailored acidolytic media when it is desirable to accelerate their deconstruction via mechanochemical bond activation. For instance, the time to full disintegration of PDK **3** in 5.0 M H_2SO_4 and 5.0 M HCl was seven and three times longer than that in 5.0 M HBr, respectively. Thus, the density of cleavable bonds within the network controls the rate at which bulk solids transform into smaller dispersed solids, allowing process 2 to proceed at rates dictated by the surface area and the aforementioned polymer interactions with the acidolytic reaction medium vis-à-vis bond activation, water activity toward hydrolysis reactions, and water residence time near hydrolyzable bonds.

In large reactors, where such transformations will eventually take place, stirring rates and residence times affect energy requirements for executing circularity at scale. The physical mechanisms described here are a means to tailor these to minimize such costs in the future, provided that there are no discernable differences in the quality of recyclates produced by comparison to first-generation monomers. To verify this, we analyzed the purities and quantified the yields of TK **1** and triamine cross-linkers **1** to **3** recovered from deconstructed elastomeric PDK **1** to **3**, respectively, in each of the three acidolytic reaction media (fig. S18). In all cases, recovered TK **1** and triamine **1** to **3** were essentially indistinguishable from pristine monomers by ^{1}H NMR (Fig. 4, C and D, and fig. S19 to S27). The recovery yields were >90% with no obvious distinction between different acids. Thus, the interactions with polymers and acidolytic reaction media during polymer deconstruction can be tailored to more quickly generate higher–surface area particulates that are easier to distribute within a reactor with stirring, such that subsequent monomer generation in the final stages of hydrolysis benefits from the increased surface area. More specifically, the first process of network deconstruction can be accelerated by mechanochemical effects tied to the degree of swelling, while the second process can be accelerated by bond activation in solvent-separated ion pairs.

DISCUSSION

Deconstruction of polymer networks in acidolytic media reveals distinctive roles at different timescales and length scales played by network architecture and acid counterions. At early stages of deconstruction of macroscopic polymer solids, solvation and swelling of the network predominantly lead to an acceleration of deconstruction rates due to mechanochemical activation of hydrolyzable bonds. Network swelling is enhanced for acid anions with increasing chaotropicity, resulting in initial rates that are more than sixfold higher than those for small-molecule analogs. As deconstruction proceeds, the influence of the reaction medium remains prominent due to the activation of hydrolyzable bonds at the molecular scale, particularly in solvent-separated ion pairs; the activity of water also changes substantially with acid composition at high concentrations, affecting rates in a manner that is matched to those of bond activation with different acid anions. These molecular-scale phenomena not only alter energy landscapes for bond hydrolysis ($\Delta\Delta G^{\ddagger}$ up to 3 kJ mol^{-1}) but also affect the water residence time near activated bonds and therefore the statistics of reactions producing reusable monomers. Thus, polymer-solvent interactions must be explicitly taken into account alongside monomer design when considering the fundamental and practical basis for recycling efficiency and circularity in plastics. Moreover, these interactions can now be accounted for by implementing workflows that combine synthetic chemistry, advanced in situ characterization, and computational simulations at their relevant length scales and timescales.

MATERIALS AND METHODS

Materials

5,5-Dimethyl-1,3-cyclohexanedione (95%), *N*,*N*′-dicyclohexylcarbodiimide (99%), 4-(dimethylamino)pyridine (>99%), acetic acid (>99%), and 2,5-dihydroxybenzoic acid (super DHB) were purchased from Sigma-Aldrich and used as received. Sebacic acid (99%) was purchased from Arkema and used as received. Trimethylolpropane *tris*[poly(propylene glycol), amine terminated] ether (triamine **1**, avg. molar mass of 440 g mol^{-1}) and propane-1,2,3-triol *tris*[poly(propylene glycol), amine terminated] ether (triamine **2**, avg. molar mass of 3000 g mol^{-1}; triamine **3**, avg. molar mass of 5000 g mol^{-1}) were obtained from Huntsman and used as received. 1-Methoxy-2-propylamine was purchased from ChemCruz and used as received. All solvents [dichloromethane (DCM) (99%), tetrahydrofuran (THF) (99%), ethyl acetate (99%), and methanol (99.8%)] were purchased from VWR and used without further purification. All mineral acids was purchased from Sigma-Aldrich and used without further purification. SiNx membranes with a square window were purchased from Norcada and used as received.

Methods

NMR spectroscopy

^{1}H and ^{13}C NMR spectroscopy was carried out using a Bruker Avance II at 500 MHz. Chemical shifts are reported in δ (parts per million) relative to the residual solvent peak: $CDCl_3$: 7.26 for ^{1}H. Splitting patterns are designated as s (singlet), d (doublet), t (triplet), q (quartet), and m (multiplet).

Fourier transform infrared spectra (FTIR)

Data were acquired using Thermo Fisher Scientific Nicolet iS50 spectrometer in attenuated total reflectance mode. Analytes were dissolved in THF, then drop casted on the diamond window, and allowed to completely dry before starting the recording of spectrum.

Differential scanning calorimetry

Data were acquired using a TA Instruments Q200 differential scanning calorimeter. Samples were heated over a temperature range of 40° to 280°C at a rate of 10°C min^{-1} for the heating step and 50°C min^{-1} for the cooling step under N_2 atmosphere. For each sample, data acquisition runs consisted of a heating step, a cooling step, and a second heating step. Glass transition temperatures (T_g) were interpreted and reported from the second heating curve.

Thermogravimetric analysis

Thermogravimetric analysis was performed on a TA instruments TGA5500 thermal analyzer. First, samples were heated under nitrogen from 20° to 150°C and held at 150°C for 60 min. Then, the samples were heated under nitrogen at a rate of 10°C min^{-1} from 20° to 800°C. Mass loss and degradation temperatures were interpreted and reported from the second heating ramp.

Matrix-assisted laser desorption/ionization–time-of-flight mass spectrometry

Matrix-assisted laser desorption/ionization–Time-of-flight (MALDI–ToF) mass spectra were recorded using a Bruker rapifleX spectrometer in positive reflector mode. A solution containing an analyte (5 mg ml^{-1}) and super DHB (20 mg ml^{-1}) was separately prepared in DCM and combined in a 1:1 ratio before sample deposition. One

microliter of this mixture was applied to a stainless steel target plate and allowed to dry completely before analysis.

Rheological analysis

Rheological characterizations including amplitude sweep, frequency sweep, and stress relaxation was carried out using a TA DHR-2 rheometer. PDK elastomer samples were cut into 8-mm discs with a biopsy punch and loaded onto a rheometer between 8-mm stainless steel parallel plates.

Uniaxial tensile testing

Uniaxial tensile measurements were carried out using an Instron 68TM-5 with a 1-kN load cell at ambient temperature with a strain rate of 50 mm min^{-1}. Dog bone samples following the ASTM D638 type V standard was cut using a stainless steel die.

Near-edge x-ray absorption fine structure

NEXAFS was carried out at the Advanced Light Source beamline 11.0.1.2. The dry film and static liquid cell samples were mounted onto a controllable heating stage for temperature variation experiments.

Raman spectroscopy

Raman spectroscopy was performed using an Aramis confocal Raman microscope with an incidence laser wavelength of 532 nm. The sample was dissolved in a 5.0 M acid solution and dropped onto a glass slide for measurements.

Fabrication of PDK elastomers

PDK elastomers (PDK **1** to **3**) were synthesized by mixing the ditopic triketone monomer TK **1** and tritopic amine monomer triamines **1** to **3** separately in DCM using a vortex mixer followed by subsequent curing and solvent evaporation under 60°C. The amine-to-triketone molar equivalence was kept at 1.3, and the solvent–to–total monomer weight ratio was kept at 1 for all formulations. Typically, for the fabrication of PDK **1** elastomer, 1 g of TK **1** was first dissolved in 1 g of DCM and 0.94 g of triamine **1** was dissolved in 0.94 g of DCM; the two solutions were mixed in a scintillating vial. After stirring using a vortex mixer for 30 s, the solution became viscous and was poured into a polytetrafluoroethylene (PTFE) mold. The subsequent curing of the elastomer and evaporation of the solvent was carried out at 60°C overnight.

To reshape the PDK elastomers for subsequent characterization, the cured PDK elastomer was hot pressed into sheets with a thickness of ~1 mm using a PTFE mold at 150°C under 60 psi of pressure. Samples were cropped out of the PDK sheet into various shapes using stainless steel dies for uniaxial tensile testing, rheological measurements, and bulk depolymerization tests.

Fabrication of NEXAFS samples

PDK elastomers (PDK **1**) were spin coated onto the SiNx windows from a dilute precursor solution with a spin rate of 3000 rpm using a SCS 6800 spin coater. The precursor solution was prepared by dissolving 10 mg of ditopic triketone monomer TK **1** and 9.4 mg of tritopic amine monomer triamine **1** in 1 g of THF.

For dry film samples, the PDK elastomer was spin coated onto a 5- × 5-mm SiNx window with a window size of 1.5 × 1.5 mm. The spin-coated sample was thermally annealed at 60°C for 2 hours before used for testing.

For static liquid cell samples, the PDK elastomer was first spin coated onto a 7.5- × 7.5-mm frame SiNx window with a window size of 1 × 0.3 mm. The spin-coated sample was then thermally annealed at 60°C for 2 hours to fully cure the elastomer. Subsequently, the PDK elastomer thin film in the region outside of the window area was carefully removed using a razor blade. A 0.3-μl 5.0 M H_2SO_4/HCl/HBr solution was then dropped onto the window area. Last, another SiNx window with the frame dimension of 5 × 5 mm was carefully closed over the first window with the window area aligned, sandwiching the acid solution and PDK thin film in the cell. Norland NOA68T epoxy was then applied over the edge of the second window, and the epoxy was cured by irradiating with a handheld ultraviolet lamp for 2 min to create an airtight seal. The static liquid cell samples were immediately transferred into the testing chamber for characterization.

Acid-catalyzed hydrolytic depolymerization of PDK elastomers

The hot-pressed PDK elastomers were cut into rectangular sheets with a dimension of around 10 (W) × 20 (H) × 1 (T) mm. The weight of each piece of PDK before depolymerization was recorded for subsequent yield calculations during recovery of the monomers. The PDK rectangle was immersed in 12 ml of 5.0 M H_2SO_4/HCl/HBr in a 20-ml scintillating vial and allowed to depolymerize up to 96 hours at 60°C with gentle stirring.

Recovery of TK 1 and triamine 1 to 3 monomers from PDK elastomers

The mixture of depolymerized PDK was first cooled down to 4°C and then filtered to separate the TK **1** precipitate and the triamine dissolved in an acid solution.

To recover the triketone monomers, the retentate was first washed once with the same type of acid used during depolymerization and then washed two times with deionized water. The retentate was then dried under vacuum to yield an off-white solid. The crude recovered solid was then purified by recrystallizing in ethanol. The purity of the recovered TK **1** was verified by ^{1}H NMR. The recovery yield was calculated by dividing the weight of recovered TK **1** to the theoretical weight of TK **1** in the PDK sample used for depolymerization.

To recover the triamine monomers, the clear filtrate was first basified to pH 14 using 2.0 M KOH solutions. The filtrate turned slightly cloudy, with oily aggregates formed on the surface of the solution. The basified filtrate was then extracted using DCM. The organic phase was retained and dried under reduced pressure to yield a yellow viscous oil. The purity of the recovered triamines **1** to **3** was verified by ^{1}H NMR and MALDI–ToF spectrometry. The recovery yield was calculated by comparing the weight of recovered triamine to the theoretical weight of triamine in the PDK sample used for depolymerization.

Supplementary Materials

This PDF file includes:

Supplementary Text
Figs. S1 to S27
Tables S1 to S5
References

REFERENCES AND NOTES

1. G. W. Coates, Y. D. Y. L. Getzler, Chemical recycling to monomer for an ideal, circular polymer economy. *Nat. Rev. Mater.* **5**, 501–516 (2020).
2. B. A. Abel, R. L. Snyder, G. W. Coates, Chemically recyclable thermoplastics from reversible-deactivation polymerization of cyclic acetals. *Science* **373**, 783–789 (2021).
3. M. Häußler, M. Eck, D. Rothauer, S. Mecking, Closed-loop recycling of polyethylene-like materials. *Nature* **590**, 423–427 (2021).
4. D. Sathe, J. Zhou, H. Chen, H.-W. Su, W. Xie, T.-G. Hsu, B. R. Schrage, T. Smith, C. J. Ziegler, J. Wang, Olefin metathesis-based chemically recyclable polymers enabled by fused-ring monomers. *Nat. Chem.* **13**, 743–750 (2021).
5. L. Zhou, Z. Zhang, C. Shi, M. Scoti, D. K. Barange, R. R. Gowda, E. Y. X. Chen, Chemically circular, mechanically tough, and melt-processable polyhydroxyalkanoates. *Science* **380**, 64–69 (2023).
6. X. Wang, S. Zhan, Z. Lu, J. Li, X. Yang, Y. Qiao, Y. Men, J. Sun, Healable, recyclable, and mechanically tough polyurethane elastomers with exceptional damage tolerance. *Adv. Mater.* **32**, e2005759 (2020).

7. L. P. Manker, G. R. Dick, A. Demongeot, M. A. Hedou, C. Rayroud, T. Rambert, M. J. Jones, I. Sulaeva, M. Vieli, Y. Leterrier, A. Potthast, F. Maréchal, V. Michaud, H.-A. Klok, J. S. Luterbacher, Sustainable polyesters via direct functionalization of lignocellulosic sugars. *Nat. Chem.* **14**, 976–984 (2022).
8. P. R. Christensen, A. M. Scheuermann, K. E. Loeffler, B. A. Helms, Closed-loop recycling of plastics enabled by dynamic covalent diketoenamine bonds. *Nat. Chem.* **11**, 442–448 (2019).
9. B. A. Helms, Polydiketoenamines for a circular plastics economy. *Acc. Chem. Res.* **55**, 2753–2765 (2022).
10. A. R. Epstein, J. Demarteau, B. A. Helms, K. A. Persson, Variable amine spacing determines depolymerization rate in polydiketoenamines. *J. Am. Chem. Soc.* **145**, 8082–8089 (2023).
11. J. Demarteau, A. R. Epstein, P. R. Christensen, M. Abubekerov, H. Wang, S. J. Teat, T. J. Seguin, C. W. Chan, C. D. Scown, T. P. Russell, J. D. Keasling, K. A. Persson, B. A. Helms, Circularity in mixed-plastic chemical recycling enabled by variable rates of polydiketoenamine hydrolysis. *Sci. Adv.* **8**, eabp8823 (2022).
12. J. Demarteau, B. Cousineau, Z. Wang, B. Bose, S. Cheong, G. Lan, N. R. Baral, S. J. Teat, C. D. Scown, J. D. Keasling, B. A. Helms, Biorenewable and circular polydiketoenamine plastics. *Nat. Sustain.* **6**, 1426–1435 (2023).
13. J. B. Young, R. W. Hughes, A. M. Tamura, L. S. Bailey, K. A. Stewart, B. S. Sumerlin, Bulk depolymerization of poly(methyl methacrylate) via chain-end initiation for catalyst-free reversion to monomer. *Chem* **9**, 2669–2682 (2023).
14. L. D. Ellis, N. A. Rorrer, K. P. Sullivan, M. Otto, J. E. McGeehan, Y. Román-Leshkov, N. Wierckx, G. T. Beckham, Chemical and biological catalysis for plastics recycling and upcycling. *Nat. Catal.* **4**, 539–556 (2021).
15. M. Chu, Y. Liu, X. Lou, Q. Zhang, J. Chen, Rational design of chemical catalysis for plastic recycling. *ACS Catal.* **12**, 4659–4679 (2022).
16. D. J. Buckley, S. B. Robison, Ozone attack on rubber vulcanizates. *J. Polym. Sci.* **19**, 145–158 (1956).
17. R. L. Zapp, J. H. Peery, The ozone attack on swollen elastomeric networks. *J. Appl. Polym. Sci.* **13**, 2097–2112 (1969).
18. F. K. Metze, S. Sant, Z. Meng, H.-A. Klok, K. Kaur, Swelling-activated, soft mechanochemistry in polymer materials. *Langmuir* **39**, 3546–3557 (2023).
19. C. K. Lee, C. E. Diesendruck, E. Lu, A. N. Pickett, P. A. May, J. S. Moore, P. V. Braun, Solvent swelling activation of a mechanophore in a polymer network. *Macromolecules* **47**, 2690–2694 (2014).
20. A. E. M. Beedle, M. Mora, C. T. Davis, A. P. Snijders, G. Stirnemann, S. Garcia-Manyes, Forcing the reversibility of a mechanochemical reaction. *Nat. Commun.* **9**, 3155 (2018).
21. J. Wang, X. Gao, A. Boarino, F. Célerse, C. Corminboeuf, H. A. Klok, Mechanical acceleration of ester bond hydrolysis in polymers. *Macromolecules* **55**, 10145–10152 (2022).
22. Y. Zhang, S. Furyk, D. E. Bergbreiter, P. S. Cremer, Specific ion effects on the water solubility of macromolecules: PNIPAM and the Hofmeister series. *J. Am. Chem. Soc.* **127**, 14505–14510 (2005).
23. E. E. Bruce, N. F. A. Van Der Vegt, Molecular scale solvation in complex solutions. *J. Am. Chem. Soc.* **141**, 12948–12956 (2019).
24. Z. He, W. J. Xie, Z. Liu, G. Liu, Z. Wang, Y. Q. Gao, J. Wang, Tuning ice nucleation with counterions on polyelectrolyte brush surfaces. *Sci. Adv.* **2**, e1600345 (2016).
25. Q. Guo, Z. He, Y. Jin, S. Zhang, S. Wu, G. Bai, H. Xue, Z. Liu, S. Jin, L. Zhao, J. Wang, Tuning ice nucleation and propagation with counterions on multilayer hydrogels. *Langmuir* **34**, 11986–11991 (2018).
26. Z. He, C. Wu, M. Hua, S. Wu, D. Wu, X. Zhu, J. Wang, X. He, Bioinspired multifunctional anti-icing hydrogel. *Matter* **2**, 723–734 (2020).
27. H. Zhang, W. Wang, S. Mallapragada, A. Travesset, D. Vaknin, Ion-specific interfacial crystallization of polymer-grafted nanoparticles. *J. Phys. Chem. C* **121**, 15424–15429 (2017).
28. S. Wu, C. Zhu, Z. He, H. Xue, Q. Fan, Y. Song, J. S. Francisco, X. C. Zeng, J. Wang, Ion-specific ice recrystallization provides a facile approach for the fabrication of porous materials. *Nat. Commun.* **8**, 15154 (2017).
29. M. Hua, S. Wu, Y. Ma, Y. Zhao, Z. Chen, I. Frenkel, J. Strzalka, H. Zhou, X. Zhu, X. He, Strong tough hydrogels via the synergy of freeze-casting and salting out. *Nature* **590**, 594–599 (2021).
30. J. Resasco, L. D. Chen, E. Clark, C. Tsai, C. Hahn, T. F. Jaramillo, K. Chan, A. T. Bell, Promoter effects of alkali metal cations on the electrochemical reduction of carbon dioxide. *J. Am. Chem. Soc.* **139**, 11277–11287 (2017).
31. H. Zhang, J. Gao, D. Raciti, A. S. Hall, Promoting Cu-catalysed CO_2 electroreduction to multicarbon products by tuning the activity of H_2O. *Nat. Catal.* **6**, 807–817 (2023).
32. E. A. Dailing, P. Khanal, A. R. Epstein, J. Demarteau, K. A. Persson, B. A. Helms, Circular polydiketoenamine elastomers with exceptional creep resistance via multivalent cross-linker design. *ACS Cent. Sci.* **10**, 54–64 (2024).
33. Huntsman Corporation (HUN), Polyetheramines, https://huntsman.com/products/detail/354/polyetheramines.
34. K. W. Harrison, D. Murtagh, H. Silva, J. G. Cordaro, "Thermal degradation investigation of polyurethane elastomers using thermal gravimetric analysis–gas chromatography/mass spectrometry"(report no. SAND-2017-0645, 2017); https://osti.gov/servlets/purl/1505419.
35. E. Darroman, N. Durand, B. Boutevin, S. Caillol, Improved cardanol derived epoxy coatings. *Prog. Org. Coat.* **91**, 9–16 (2016).
36. J. Timoshenko, B. Roldan Cuenya, In situ/operando electrocatalyst characterization by X-ray absorption spectroscopy. *Chem. Rev.* **121**, 882–961 (2021).
37. X. Chen, T. Yang, S. Kataoka, P. S. Cremer, Specific ion effects on interfacial water structure near macromolecules. *J. Am. Chem. Soc.* **129**, 12272–12279 (2007).
38. N. Ghosh, S. Roy, A. Bandyopadhyay, J. A. Mondal, Vibrational raman spectroscopy of the hydration shell of ions. *Liquids* **3**, 19–39 (2023).
39. J. L. Fulton, M. Balasubramanian, Structure of hydronium (H_3O^+)/chloride (Cl^-) contact ion pairs in aqueous hydrochloric acid solution: A Zundel-like local configuration. *J. Am. Chem. Soc.* **132**, 12597–12604 (2010).
40. Q. Sun, The Raman OH stretching bands of liquid water. *Vib. Spectrosc.* **51**, 213–217 (2009).
41. Y.-H. Wang, S. Zheng, W.-M. Yang, R.-Y. Zhou, Q.-F. He, P. Radjenovic, J.-C. Dong, S. Li, J. Zheng, Z.-L. Yang, G. Attard, F. Pan, Z.-Q. Tian, J.-F. Li, In situ Raman spectroscopy reveals the structure and dissociation of interfacial water. *Nature* **600**, 81–85 (2021).
42. M. Ahmed, V. Namboodiri, A. K. Singh, J. A. Mondal, S. K. Sarkar, How ions affect the structure of water: A combined Raman spectroscopy and multivariate curve resolution study. *J. Phys. Chem. B* **117**, 16479–16485 (2013).
43. M. J. Blandamer, J. B. F. N. Engberts, P. T. Gleeson, J. C. R. Reis, Activity of water in aqueous systems; A frequently neglected property. *Chem. Soc. Rev.* **34**, 440–458 (2005).
44. X. Man, M. Doi, Swelling dynamics of a disk-shaped gel. *Macromolecules* **54**, 4626–4632 (2021).
45. S. Hirata, M. Head-Gordon, Time-dependent density functional theory within the Tamm–Dancoff approximation. *Chem. Phys. Lett.* **314**, 291–299 (1999).
46. R. L. Gieseking, M. A. Ratner, G. C. Schatz, Semiempirical modeling of Ag nanoclusters: New parameters for optical property studies enable determination of double excitation contributions to plasmonic excitation. *J. Phys. Chem. A* **120**, 4542–4549 (2016).
47. E. Epifanovsky, A. T. B. Gilbert, X. Feng, J. Lee, Y. Mao, N. Mardirossian, P. Pokhilko, A. F. White, M. P. Coons, A. L. Dempwolff, Z. Gan, D. Hait, P. R. Horn, L. D. Jacobson, I. Kaliman, J. Kussmann, A. W. Lange, K. U. Lao, D. S. Levine, J. Liu, S. C. McKenzie, A. F. Morrison, K. D. Nanda, F. Plasser, D. R. Rehn, M. L. Vidal, Z.-Q. You, Y. Zhu, B. Alam, B. J. Albrecht, A. Aldossary, E. Alguire, J. H. Andersen, V. Athavale, D. Barton, K. Begam, A. Behn, N. Bellonzi, Y. A. Bernard, E. J. Berquist, H. G. A. Burton, A. Carreras, K. Carter-Fenk, R. Chakraborty, A. D. Chien, K. D. Closser, V. Cofer-Shabica, S. Dasgupta, M. De Wergifosse, J. Deng, M. Diedenhofen, H. Do, S. Ehlert, P.-T. Fang, S. Fatehi, Q. Feng, T. Friedhoff, J. Gayvert, Q. Ge, G. Gidofalvi, M. Goldey, J. Gomes, C. E. González-Espinoza, S. Gulania, A. O. Gunina, M. W. D. Hanson-Heine, P. H. P. Harbach, A. Hauser, M. F. Herbst, M. H. Vera, M. Hodecker, Z. C. Holden, S. Houck, X. Huang, K. Hui, B. C. Huynh, M. Ivanov, Á. Jász, H. Ji, H. Jiang, B. Kaduk, S. Kähler, K. Khistyaev, J. Kim, G. Kis, P. Klunzinger, Z. Koczor-Benda, J. H. Koh, D. Kosenkov, L. Koulias, T. Kowalczyk, C. M. Krauter, K. Kue, A. Kunitsa, T. Kus, I. Ladjánszki, A. Landau, K. V. Lawler, D. Lefrancois, S. Lehtola, R. R. Li, Y.-P. Li, J. Liang, M. Liebenthal, H.-H. Lin, Y.-S. Lin, F. Liu, K.-Y. Liu, M. Loipersberger, A. Luenser, A. Manjanath, P. Manohar, E. Mansoor, S. F. Manzer, S.-P. Mao, A. V. Marenich, T. Markovich, S. Mason, S. A. Maurer, P. F. McLaughlin, M. F. S. J. Menger, J.-M. Mewes, S. A. Mewes, P. Morgante, J. W. Mullinax, K. J. Oosterbaan, G. Paran, A. C. Paul, S. K. Paul, F. Pavošević, Z. Pei, S. Prager, E. I. Proynov, Á. Rák, E. Ramos-Cordoba, B. Rana, A. E. Rask, A. Rettig, R. M. Richard, F. Rob, E. Rossomme, T. Scheele, M. Scheurer, M. Schneider, N. Sergueev, S. M. Sharada, W. Skomorowski, D. W. Small, C. J. Stein, Y.-C. Su, E. J. Sundstrom, Z. Tao, J. Thirman, G. J. Tornai, T. Tsuchimochi, N. M. Tubman, S. P. Veccham, O. Vydrov, J. Wenzel, J. Witte, A. Yamada, K. Yao, S. Yeganeh, S. R. Yost, A. Zech, I. Y. Zhang, X. Zhang, Y. Zhang, D. Zuev, A. Aspuru-Guzik, A. T. Bell, N. A. Besley, K. B. Bravaya, B. R. Brooks, D. Casanova, J. D. Chai, S. Coriani, C. J. Cramer, G. Cserey, A. E. Deprince III, R. A. Distasio Jr., A. Dreuw, B. D. Dunietz, T. R. Furlani, W. A. Goddard III, S. Hammes-Schiffer, T. Head-Gordon, W. J. Hehre, C.-P. Hsu, T.-C. Jagau, Y. Jung, A. Klamt, J. Kong, D. S. Lambrecht, W. Liang, N. J. Mayhall, C. W. McCurdy, J. B. Neaton, C. Ochsenfeld, J. A. Parkhill, R. Peverati, V. A. Rassolov, Y. Shao, L. V. Slipchenko, T. Stauch, R. P. Steele, J. E. Subotnik, A. J. W. Thom, A. Tkatchenko, D. G. Truhlar, T. Van Voorhis, T. A. Wesolowski, K. B. Whaley, H. L. Woodcock III, P. M. Zimmerman, S. Faraji, P. M. W. Gill, M. Head-Gordon, J. M. Herbert, A. I. Krylov, Software for the frontiers of quantum chemistry: An overview of developments in the Q-Chem 5 package. *J. Chem. Phys.* **155**, 084801 (2021).
48. N. A. Besley, M. J. G. Peach, D. J. Tozer, Time-dependent density functional theory calculations of near-edge X-ray absorption fine structure with short-range corrected functionals. *Phys. Chem. Chem. Phys.* **11**, 10350–10358 (2009).
49. E. D. Glendening, D. Feller, Cation-water interactions: The $M+(H_2O)_n$ clusters for alkali metals, M = Li, Na, K, Rb, and Cs. *J. Phys. Chem.* **99**, 3060–3067 (1995).
50. P. Eastman, M. S. Friedrichs, J. D. Chodera, R. J. Radmer, C. M. Bruns, J. P. Ku, K. A. Beauchamp, T. J. Lane, L.-P. Wang, D. Shukla, T. Tye, M. Houston, T. Stich, C. Klein, M. R. Shirts, V. S. Pande, OpenMM 4: A reusable, extensible, hardware independent library for high performance molecular simulation. *J. Chem. Theory Comput.* **9**, 461–469 (2013).

51. GitHub, orionarcher/pymatgen-io-openmm: A Pymatgen IO Module for Setting Up OpenMM Simulations, https://github.com/orionarcher/pymatgen-io-openmm.
52. S. Boothroyd, P. K. Behara, O. C. Madin, D. F. Hahn, H. Jang, V. Gapsys, J. R. Wagner, J. T. Horton, D. L. Dotson, M. W. Thompson, J. Maat, T. Gokey, L.-P. Wang, D. J. Cole, M. K. Gilson, J. D. Chodera, C. I. Bayly, M. R. Shirts, D. L. Mobley, Development and benchmarking of open force field 2.0.0: The Sage small molecule force field. *J. Chem. Theory Comput.* **19**, 3251–3275 (2023).
53. W. L. Jorgensen, J. Chandrasekhar, J. D. Madura, R. W. Impey, M. L. Klein, Comparison of simple potential functions for simulating liquid water. *J. Chem. Phys.* **79**, 926–935 (1983).
54. T. A. Halgren, Merck molecular force field. I. Basis, form, scope, parameterization, and performance of MMFF94. *J. Comput. Chem.* **17**, 490–519 (1996).
55. B. J. Kirby, P. Jungwirth, Charge scaling manifesto: A way of reconciling the inherently macroscopic and microscopic natures of molecular simulations. *J. Phys. Chem. Lett.* **10**, 7531–7536 (2019).
56. D. C. Liu, J. Nocedal, On the limited memory BFGS method for large scale optimization. *Math. Program.* **45**, 503–528 (1989).
57. Z. Zhang, X. Liu, K. Yan, M. E. Tuckerman, J. Liu, Unified efficient thermostat scheme for the canonical ensemble with holonomic or isokinetic constraints via molecular dynamics. *J. Phys. Chem. A* **123**, 6056–6079 (2019).
58. R. J. Gowers, M. Linke, J. Barnoud, T. J. E. Reddy, M. N. Melo, S. L. Seyler, J. Domanski, D. L. Dotson, S. Buchoux, I. M. Kenney, O. Beckstein, MDAnalysis: A Python package for the rapid analysis of molecular dynamics simulations, in *Proceedings of the 15th Python in Science Conference* (SciPy, 2019), pp. 98–105.
59. O. A. Cohen, H. Macdermott-Opeskin, L. Lee, T. Hou, K. D. Fong, R. Kingsbury, J. Wang, K. A. Persson, SolvationAnalysis: A Python toolkit for understanding liquid solvation structure in classical molecular dynamics simulations. *J. Open Source Softw.* **8**, 5183 (2023).

Acknowledgments: We thank N. Su and Huntsman Corp. for providing the triamine monomers used in the study. **Funding:** This work was funded by the US Department of Energy, Office of Science, Office of Basic Energy Sciences, Materials Sciences and Engineering Division under contract no. DE-AC02-05-CH11231, Unlocking Chemical Circularity in Recycling by Controlling Polymer Reactivity across Scales program CUP-LBL-Helms. Work at the Molecular Foundry—including polymer synthesis, characterization, x-ray liquid cell assembly, and Raman spectroscopy characterization—was supported by the Office of Science, Office of Basic Energy Sciences, of the US Department of Energy under contract no. DE-AC02-05CH11231. Work at the Advanced Light Source—including NEXAFS—was supported by the Office of Science, Office of Basic Energy Sciences, of the US Department of Energy under the same contract. This research used the Savio computational cluster resource provided by the Berkeley Research Computing program at the University of California, Berkeley (supported by the UC Berkeley chancellor, vice chancellor for research, and chief information officer). The instrument used in this work for the pulsed-field gradient NMR (diffusion-ordered spectroscopy) is supported by the National Science Foundation under grant no. 2018784.
Author contributions: B.A.H. contributed to the conceptualization of the project. B.A.H and M.H. contributed to the design of the project. B.A.H. and J.D. contributed to the design of the PDK elastomer. M.H., Z.P., and C.W. contributed to the design, experiment, and data analysis of NEXAFS characterization. R.D.G. contributed to the TD-DFT simulations of NEXAFS spectra. X.R. contributed to the MD simulations. M.H. and K.C.N. contributed to the experiment and data analysis of Raman spectroscopy. M.H., S.H., and S.N.F. contributed to the NMR characterization and analysis. B.A.H. and M.H. contributed to visualization. B.A.H. and M.H. wrote the original draft. All authors contributed to the final draft and editing. B.A.H., C.W., K.A.P., M.B.S., and J.A.R. supervised research, provided project administration, and acquired funding. **Competing interests:** B.A.H. is an inventor on the US provisional patent application 62/587,148 and submitted by the Lawrence Berkeley National Laboratory that covers PDKs as well as aspects of their use and recovery. J.D., K.A.P., and B.A.H. are inventors on the US provisional patent application 63/390,962 submitted by the Lawrence Berkeley National Laboratory that covers elastomeric PDKs as well as aspects of their use and recovery. B.A.H. has a financial interest in Cyklos Materials and Sepion Technologies. The authors declare that they have no other competing interests. **Data and materials availability:** All data needed to evaluate the conclusions in this paper are present in the paper and/or the Supplementary Materials. Materials can be provided by the Lawrence Berkeley National Laboratory pending scientific review and a completed material transfer agreement. Requests for materials should be submitted to ipo@lbl.gov.

Submitted 10 May 2024
Accepted 12 August 2024
Published 18 September 2024
10.1126/sciadv.adq3801